

Electronic Supplementary Information

High efficient oxygen evolution catalysis achieved by NiFe oxyhydroxide clusters anchored on carbon black

Zhongke Wang,^a Yuyang Wang,^a Nan Zhang,^{*a} Lixia Ma,^a Jie Sun,^a Can Yu,^{*b} Shoujie Liu^c
and Ruibin Jiang^{*a}

^aShaanxi Key Laboratory for Advanced Energy Devices, Shaanxi Engineering Lab for Advanced Energy Technology, School of Materials Science and Engineering, Shaanxi Normal University, Xi'an 710119, China.

^bInstitute of High Energy Physics, Chinese Academy of Sciences (CAS), Beijing 100049, China.

^cSpallation Neutron Source Science Center (SNSSC), Zhongziyuan Road, Dalang, Dongguan 523803, China.

Experimental Details

Chemicals

$\text{NiCl}_2 \cdot 6\text{H}_2\text{O}$ (98%, AR, Aladdin Co., Ltd), 0.65 mmol $\text{FeCl}_3 \cdot 6\text{H}_2\text{O}$ (99%, AR, Aladdin), NaOH (99.999%, Sinopharm), carbon black (ECP-600JD). All reagents were used as received and did not require further purification. DI-water (18.25 $\text{M}\Omega \cdot \text{cm}$) was used throughout all experiments.

Catalyst Preparation

In the preparation of $\text{Ni}_{0.5}\text{Fe}_{0.5}/\text{C}$, 0.65 mmol of $\text{NiCl}_2 \cdot 6\text{H}_2\text{O}$ and 0.65 mmol of $\text{FeCl}_3 \cdot 6\text{H}_2\text{O}$ were dissolved in 5 mL of DI-water and formed uniform solution. Then, 0.0444 g of untreated carbon black was added into the solution, followed by the addition of 2.6 mmol of NaOH. The obtained mixture was stirred for 30 minutes. Afterwards, the mixture was freeze-dried. Finally, the precipitations were centrifuged and washed with DI-water for three times. The electrocatalysts were obtained through drying the precipitations at 60 °C in a vacuum oven overnight. Other samples, including $\text{Ni}_{0.3}\text{Fe}_{0.7}/\text{C}$ and $\text{Ni}_{0.7}\text{Fe}_{0.3}/\text{C}$, were prepared with the same strategy by tuning the molar ratio between Fe and Ni precursors, while keeping the total metal moles of 1.3 mmol. The C- $\text{Ni}_{0.5}\text{Fe}_{0.5}/\text{C}$ sample was obtained by the calcination the $\text{Ni}_{0.5}\text{Fe}_{0.5}/\text{C}$ at 400 °C in Ar atmosphere for 2 h. The preparation of $\text{Ni}_{0.5}\text{Fe}_{0.5}$ is similar to that of $\text{Ni}_{0.5}\text{Fe}_{0.5}/\text{C}$ but without carbon black. Monometal samples, including Ni-OH/C and Fe-OH/C, were prepared with the sample procedure as $\text{Ni}_{0.5}\text{Fe}_{0.5}/\text{C}$ but with only one metal precursor.

Characterization

X-ray diffraction (XRD) patterns were obtained on Rigaku SmartLab diffractometer at 40 kV with Cu $\text{K}\alpha$ radiation ($\lambda = 1.54 \text{ \AA}$). Scanning electrons microscope (SEM) imaging was conducted on Hitachi 8200 field-emission gun scanning electron microscope with an

accelerating voltage of 5.0 kV. Transmission electron microscopy (TEM) and selected area electron diffraction (SAED) images were obtained on FEI G2 F20 with an acceleration voltage of 200 kV. The high-angle annular dark-field scanning transmission electron microscopy (HAADF-STEM) imaging and elemental mapping were carried out on FEI Theims Z at acceleration voltage of 200 kV. The aberration-corrected HAADF-STEM imaging was performed on JEM ARM 200 F with voltage of 200 kV. The specific surface area and pore size distribution were investigated by the Brunauer-Emmett-Teller (BET) equation and measured by nitrogen adsorption and desorption at 80 °C on ASAP 2020HD88. Four-point probe instrument (RTS-9, Guangzhou) was used to measure electric conductivity. The X-ray photoelectron spectroscopy (XPS) were evaluated on Axis Ultra spectrometer (Kratos Analytical Ltd) corrected with C 1s (284.8 eV), which equipped with a monochromatized Al K α X-ray source (1486.6 eV).

The X-ray absorption fine structure (XAFS) spectra data (Fe K-edge) were collected at 1W1B station in Beijing Synchrotron Radiation Facility (BSRF, operated at 2.5 GeV with a maximum current of 250 mA). The data were collected in fluorescence excitation mode using a Lytle detector. All samples were pelletized as disks of 13 mm in diameter and 1 mm in thickness using graphite powder as a binder. The acquired EXAFS data were processed according to the standard procedures using the Athena and Artemis implemented in the IFEFFIT software packages. The fitting was carried out according to the following procedures. The acquired EXAFS data were first processed according to the standard procedures using the ATHENA module implemented in the IFEFFIT software packages. The EXAFS spectra were obtained by subtracting the post-edge background from the overall absorption and then normalizing with respect to the edge-jump step. Subsequently, the $\chi(k)$ data were Fourier transformed to real (R) space using a hanning windows ($dk=1.0 \text{ \AA}^{-1}$) to separate the EXAFS contributions from different coordination shells. To obtain the quantitative structural

parameters around central atoms, least-squares curve parameter fitting was performed using the ARTEMIS module of IFEFFIT software packages.

Electrochemical Measurements

Electrocatalytic OER experiments were performed on an electrochemical workstation (CHI760E, CHI Instruments, Shanghai) with the traditional three-electrode system at 25 °C. The sample-coated rotating disk electrode (RDE), Ag/AgCl (immersed in saturated KCl solution), and graphite rod (3 mm in diameter) were used as working electrode, reference electrode, and counter electrode, respectively. The working electrode was prepared by dropping catalyst ink (6 μL) on glass carbon disk electrode (5 mm in diameter). The catalyst ink was obtained by ultrasonically mixing the mixture of catalyst (5 mg), DI-water (768 μL), ethanol (192 μL), and Nafion solution (40 μL , 5 wt. % in mixture of water and 2-propanol, Sigma-Aldrich) for 10 min. The potentials versus reversible hydrogen electrode (RHE) were obtained through the Equation S1:

$$E_{\text{RHE}} = E_{\text{Ag/AgCl}} + 0.059 \times \text{pH} + E^0(\text{Ag/AgCl}) \quad (\text{S1})$$

where the $E^0(\text{Ag/AgCl})$ is 0.198 V at room temperature. The yield of H_2O_2 was determined by use of rotation ring-disk electrode (RRDE, 5.5 mm in diameter) with a rotation speed of 1600 rpm. Before each electrochemical measurement, the working electrode was stabilized by several cycles of cyclic voltammetry (CV) scanning with a scan rate of 50 mV/s. The polarization curves were obtained by linear sweep voltammetry (LSV) with a scan rate of 5 mV/s from 1.2 V to 1.8 V versus RHE in Ar-saturated 1-M or 0.1-M KOH electrolyte. The solution resistance (R_s) used for iR -correction was obtained through fitting the electrochemical impedance spectroscopy (EIS). The EIS was measured at overpotential of 300 mV with the frequency range of 10 MHz–0.01 Hz. The EIS data were fitted and analyzed by use of ZView software. The catalyst was loaded on hydrophilic carbon cloth with the mass loading of 0.25 mg/cm^2 for stability test.

The electrochemical active surface areas (ECSA) of electrocatalysts were calculated from double layer capacitance as follows:

$$\text{ECSA} = \frac{C_{dl}}{C_s} \quad (\text{S2})$$

The C_{dl} is the double layer capacitance, which was derived from CV curves in faradaic potential region (1.37–1.47 V vs. RHE) with different scan rates (20, 40, 60, 80, 100 mV/s). In faradaic potential region, the currents mainly arise from the charging of the double layer, which should be linearly proportional to the ECSA. By plotting the capacitive current density ($\Delta J = J_{\text{anodic}} - J_{\text{cathodic}}$) against the scanning rate, the C_{dl} was the half of the slope obtained through linear fitting. Considering that the specific capacitance (C_s) for a flat surface is normally between 0.02–0.06 mF cm⁻²,^[1] the median value, 0.04 mF cm⁻², was used in our calculations.

The turnover of frequency (TOF) was calculated by the following equation:

$$\text{TOF} = \frac{I}{4 \times n \times F} \quad (\text{S3})$$

where the I , n , F are the current of polarization curves, the number of active sites, and Faraday constant (96485 C/mol), respectively. The factor of 1/4 represents that the formation of 1 mol oxygen requires 4 mol electrons. The number of active sites was derived from the CV curves in 1-M PBS electrolyte (pH = 7). Since no obvious redox peaks were observed on the CV curves, the surface active sites were nearly in linear relationship with the integrated voltammetric charges (cathodic and anodic) over the CV curves.^[2,3] Taking both reduction and oxidation as one-electron processes, the upper limit of the active site number can be calculated according to the following formula:

$$n = \frac{Q}{2F} \quad (\text{S4})$$

where Q is integrated voltammetric charges over the CV curves.

The electrochemical activation energy (E_a) was determined from OER experiments at different temperatures according to formula derived from Arrhenius equation:^[4]

$$\ln j = \text{const} + \frac{-E_a}{RT} \quad (\text{S5})$$

where the j , R and T are current density at overpotential of 300 mV, universal gas constant, and Kelvin temperature, respectively.

Theoretical Calculations

All theoretical calculations were performed by use of Vienna ab initio simulation (VASP) package.^[5,6] The density functional theory (DFT) plus U was employed for all calculations. The generalized gradient approximation by Perdew, Burke and Ernzerhof was employed for the exchange-correction energy.^[7] The ionic cores were described by projector-augmented wave potentials.^[8,9] The dispersion force in the adsorption was taken into consideration by use of a semiempirical DFT-D3 method proposed by Grimme.^[10] All of calculations were carried out with spin polarization. The energy cut-off is set to 500 eV. The Brillouin zone is sampled by a Monkhorst-Pack $3 \times 3 \times 1$ K-point grid. The U values of Fe and Ni were set to 4.30 and 3.80 eV, respectively.^[11,12] All the geometries were fully optimized until the atomic forces and energy were smaller than 0.02 eV \AA^{-1} and 10^{-5} eV , respectively. The catalysts were modeled by metal oxyhydroxide cluster supported on single-layer (1×1) graphite supercell. The vertical separation between the successive slabs was set at 1.5 nm. The free energy change (ΔG) is calculated from the ZPE-corrected total energies as $\Delta G = \Delta E + \Delta E_{\text{ZPE}} - T\Delta S$, where ΔE_{ZPE} , ΔS , and T are the zero-point energy difference, the entropy difference, and temperature, respectively. The room temperature (298.15 K) was used for free energy calculations.

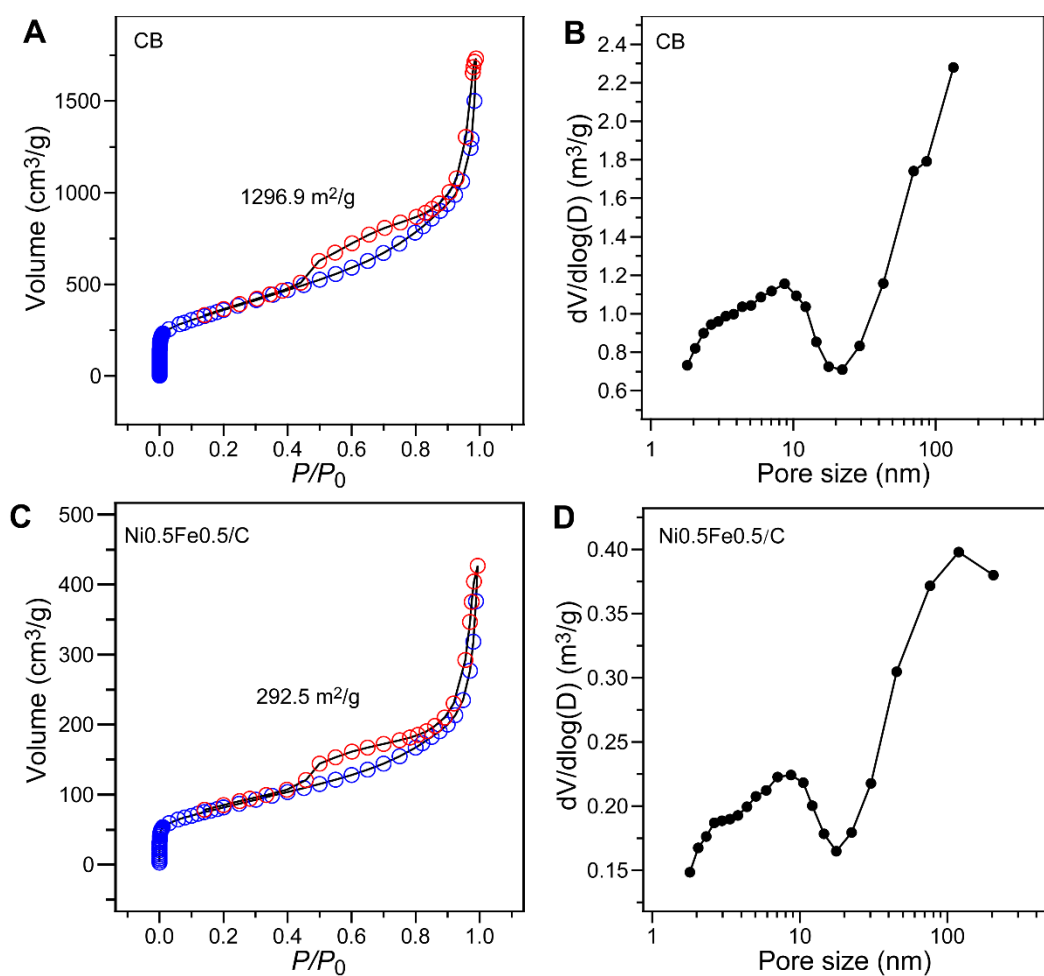


Fig. S1 A) N₂ adsorption-desorption isothermal curves of carbon black. B) Barret-Joyner-Halenda pore-size distribution curve of carbon black. C) N₂ adsorption-desorption isothermal curves of Ni_{0.5}Fe_{0.5}/C. D) Barret-Joyner-Halenda pore-size distribution curve of Ni_{0.5}Fe_{0.5}/C.

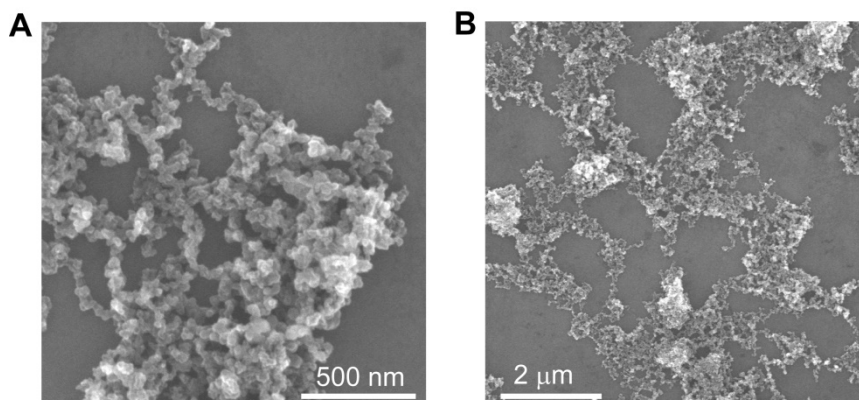


Fig. S2 A,B) SEM images of CB with different magnifications.

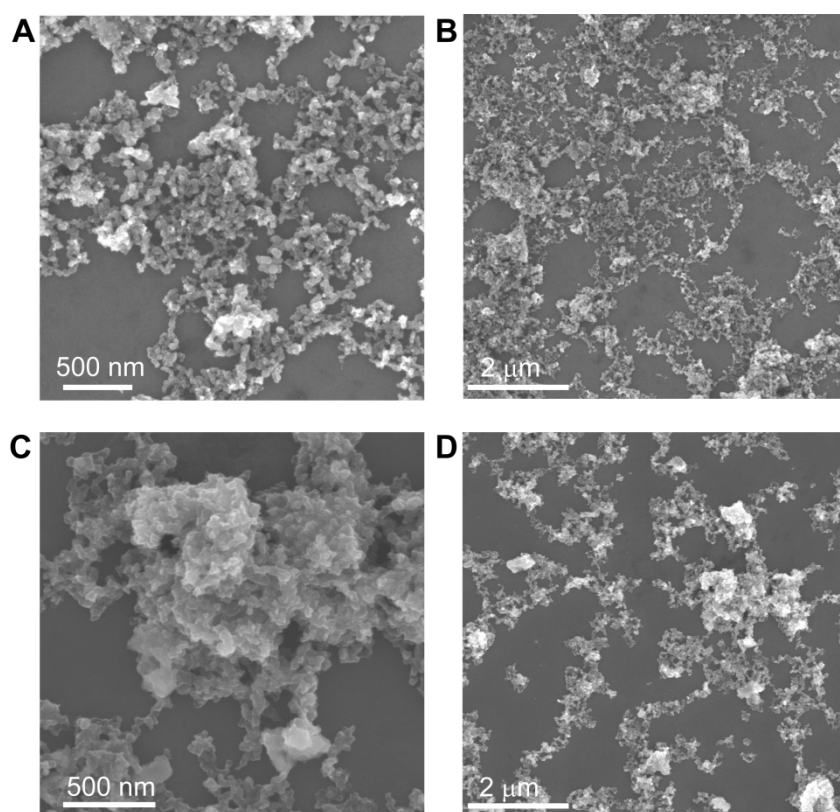


Fig. S3 SEM images of A, B) $\text{Ni}_{0.5}\text{Fe}_{0.5}/\text{C}$ and C, D) $\text{C-Ni}_{0.5}\text{Fe}_{0.5}/\text{C}$ with different magnifications.

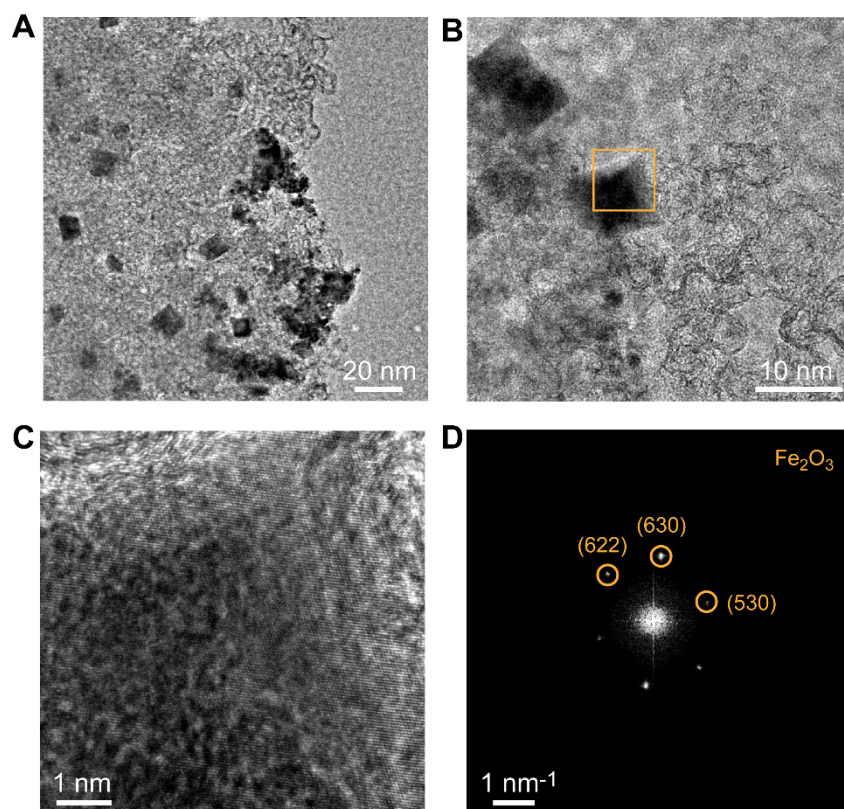


Fig. S4 A,B) Low and large magnification TEM images of $\text{C-Ni}_{0.5}\text{Fe}_{0.5}/\text{C}$, respectively. C) HRTEM image of the marked square region in (B). D) FT image of (C).

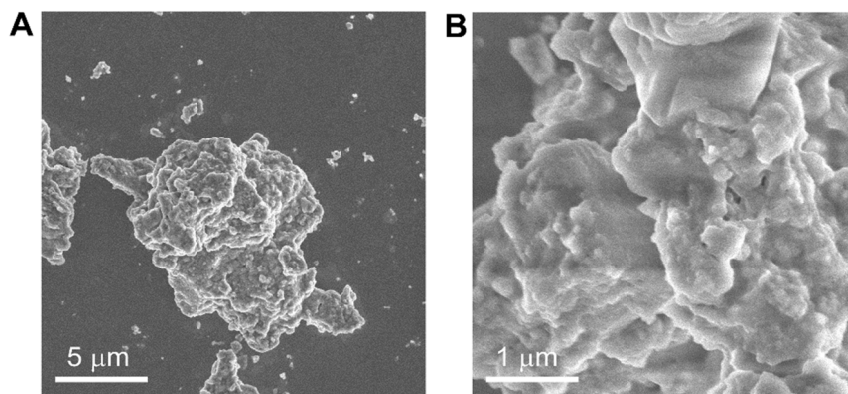


Fig. S5 SEM images of Ni_{0.5}Fe_{0.5} with different magnifications.

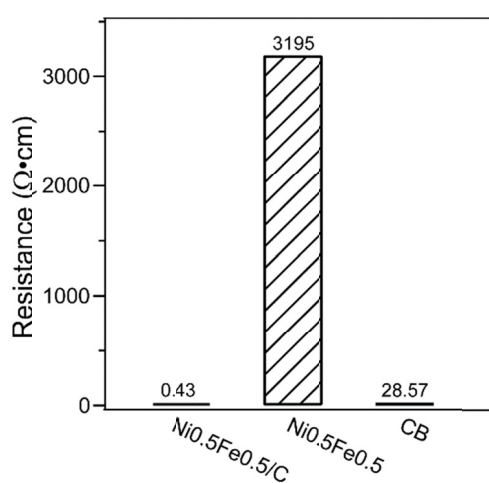


Fig. S6 Electric conductivity of Ni_{0.5}Fe_{0.5}, Ni_{0.5}Fe_{0.5}/C, and carbon black (CB).

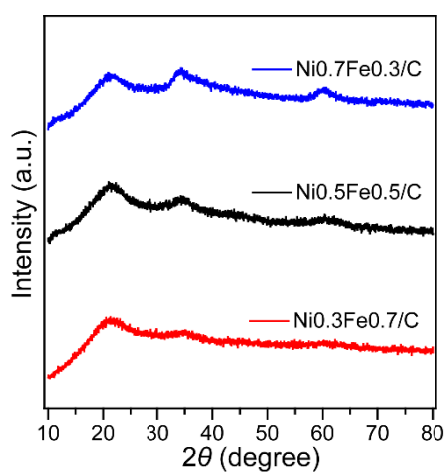


Fig. S7 XRD patterns of Ni_{0.3}Fe_{0.7}/C, Ni_{0.5}Fe_{0.5}/C, and Ni_{0.7}Fe_{0.3}/C.

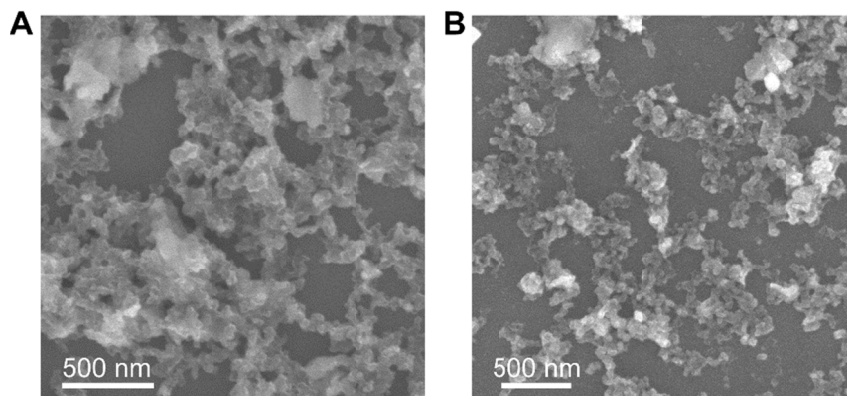


Fig. S8 A,B) SEM images of Ni_{0.7}Fe_{0.3}/C and Ni_{0.3}Fe_{0.7}/C, respectively.

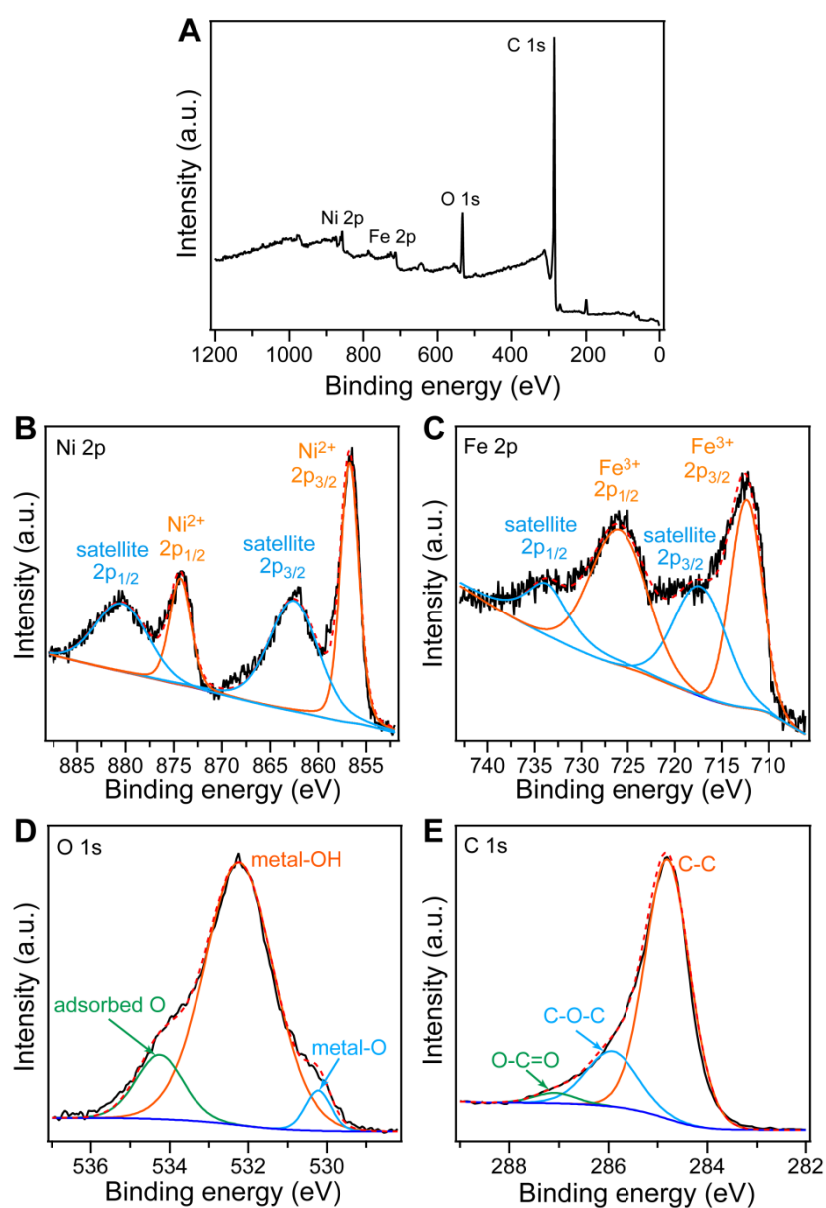


Fig. S9 A) Full, B) Ni 2p, C) Fe 2p, D) O 1s, and E) C 1s XPS spectra of Ni_{0.5}Fe_{0.5}/C.

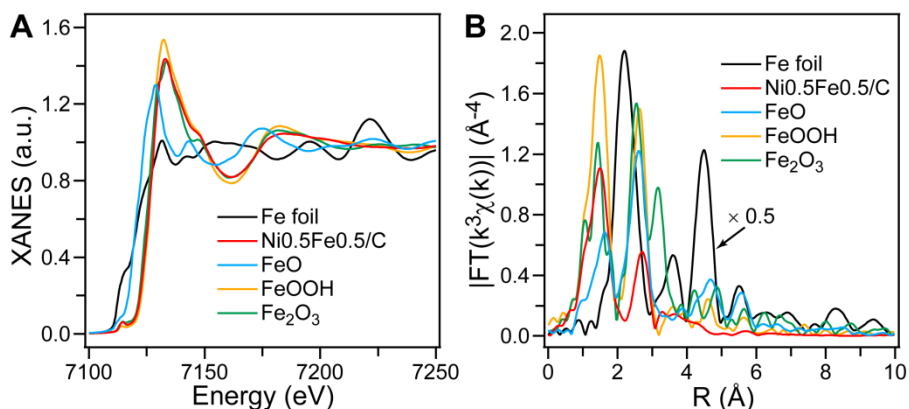


Fig. S10 A) Fe K-edge XANES spectra of Fe foil, Ni_{0.5}Fe_{0.5}/C, FeO, FeOOH, and Fe₂O₃. B) Fourier transform (FT) of k^3 -weighted Fe K-edge EXAFS spectra of Fe foil, Ni_{0.5}Fe_{0.5}/C, FeO, FeOOH, and Fe₂O₃.

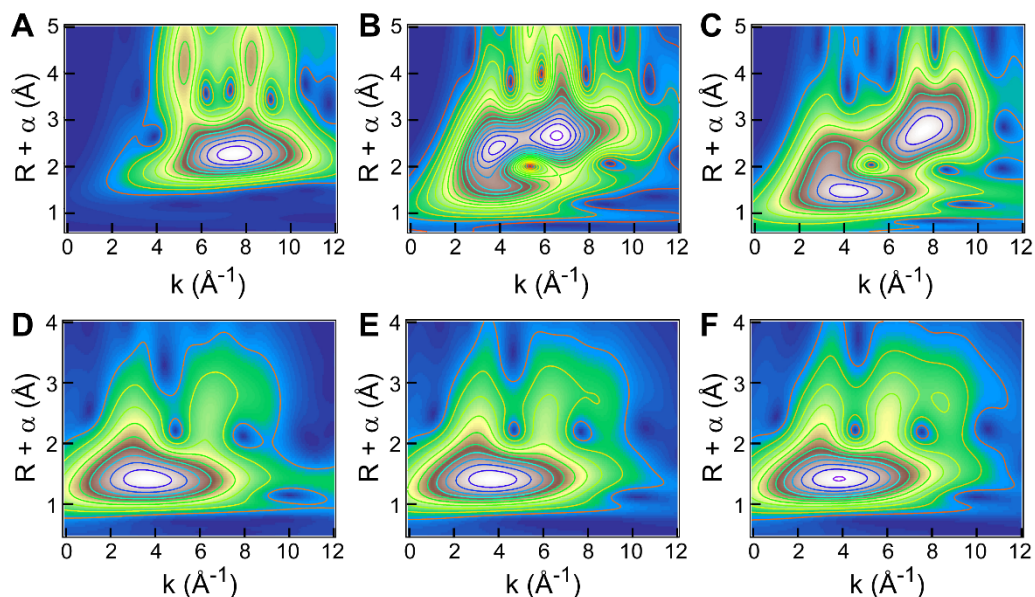


Fig. S11 WT of Fe K-edge EXAFS in A) Fe foil, B) FeO, C) Fe₂O₃, D) Ni_{0.3}Fe_{0.7}/C, E) Ni_{0.5}Fe_{0.5}/C, and F) Ni_{0.7}Fe_{0.3}/C.

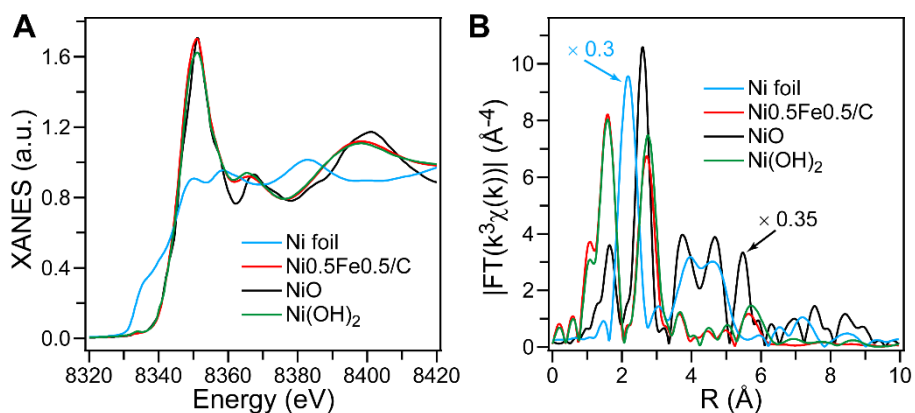


Fig. S12 A) Ni K-edge XANES spectra of Ni foil, Ni_{0.5}Fe_{0.5}/C, NiO, and Ni(OH)₂. B) Fourier transform (FT) of k^3 -weighted Fe K-edge EXAFS spectra of Ni foil, Ni_{0.5}Fe_{0.5}/C, NiO, and Ni(OH)₂.

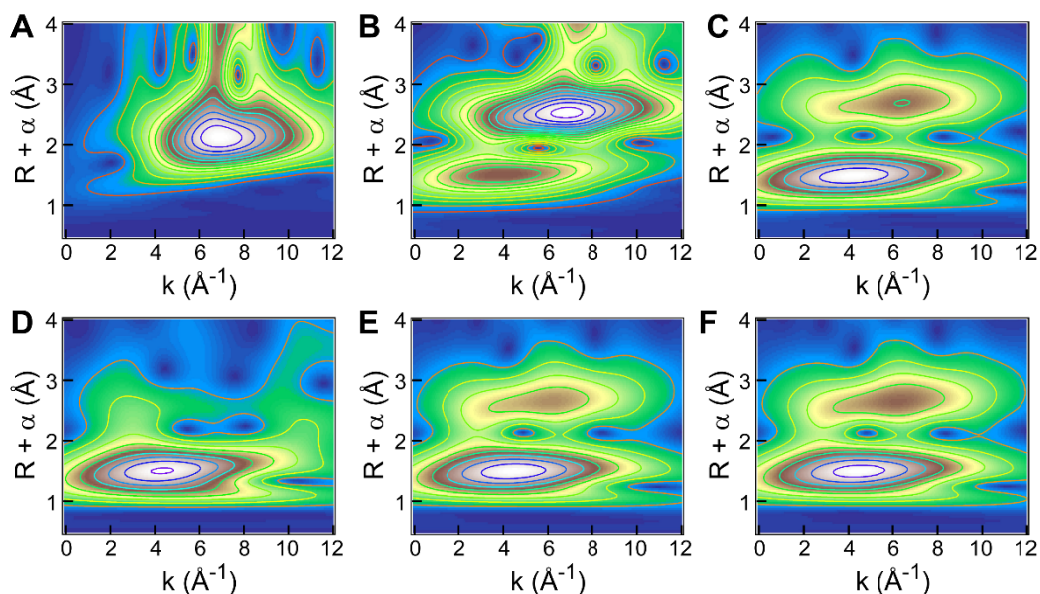


Fig. S13 WT of Ni K-edge EXAFS in A) Ni foil, B) NiO, C) Ni(OH)₂, D) Ni_{0.3}Fe_{0.7}/C, E) Ni_{0.5}Fe_{0.5}/C, and F) Ni_{0.7}Fe_{0.3}/C.

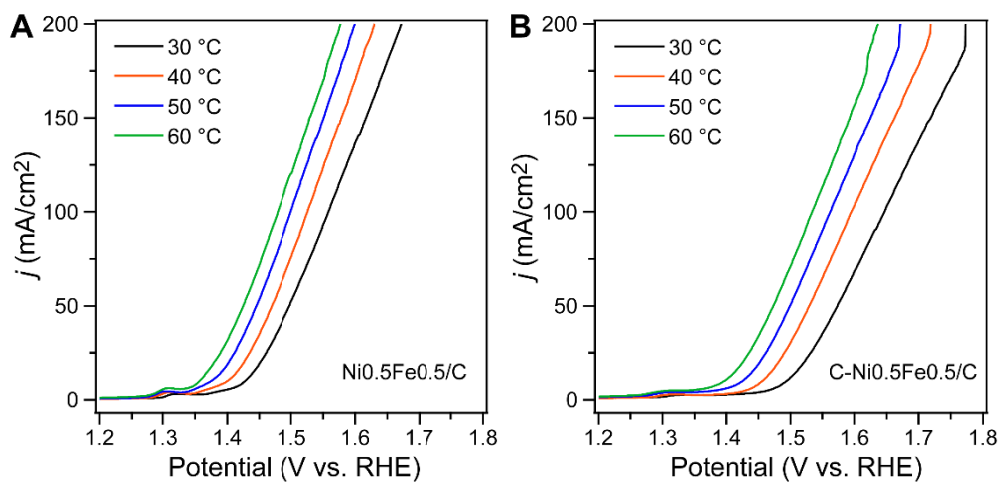


Fig. S14 Polarization curves of A) Ni_{0.5}Fe_{0.5}/C and B) C-Ni_{0.5}Fe_{0.5}/C at different temperatures.

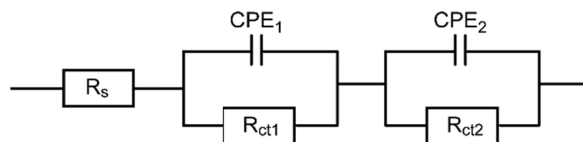


Fig. S15 Circuit used for ESI fitting.

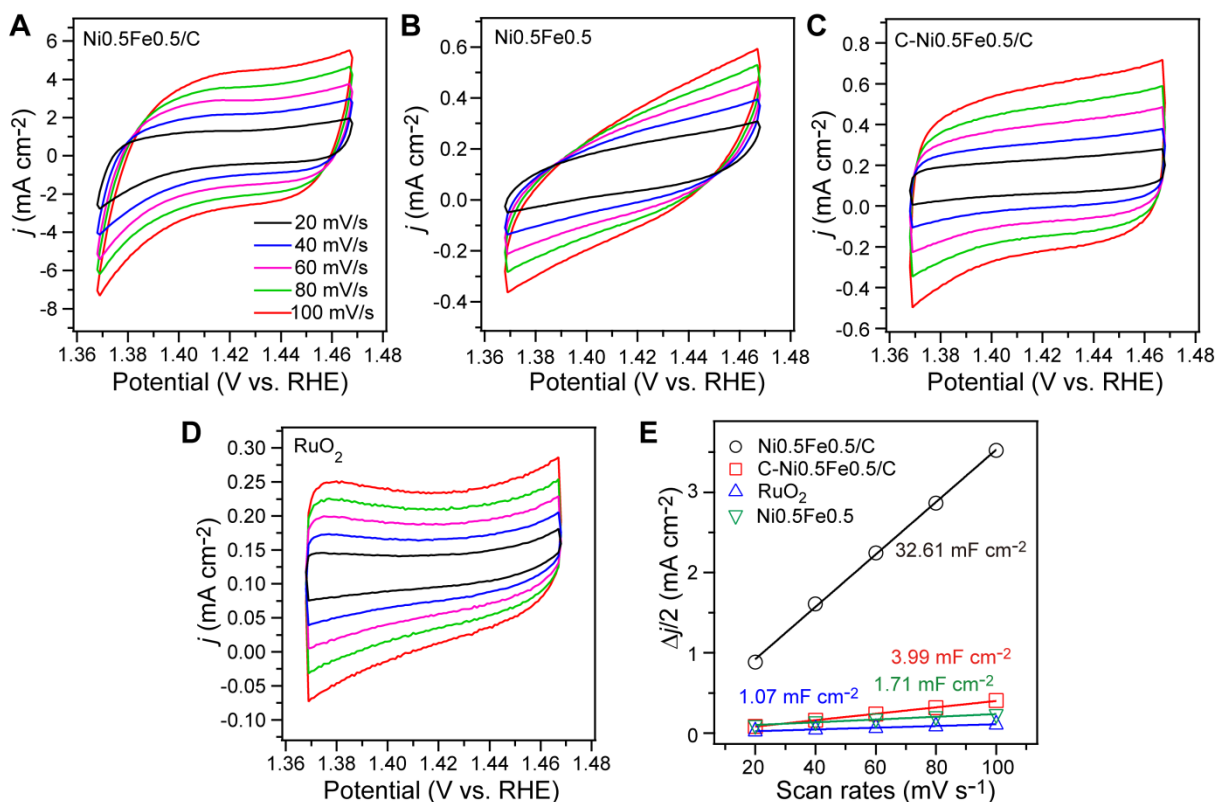


Fig. S16 Cyclic voltammetric curves of A) Ni_{0.5}Fe_{0.5}/C, B) Ni_{0.5}Fe_{0.5}, C) C-Ni_{0.5}Fe_{0.5}/C, and D) commercial RuO₂ catalyst under different scanning speeds. E) Charging current density differences plotted against scan rates. The charging current density differences are obtained at 1.42 V. The linear slope, equivalent to twice the double-layer capacitance, C_{dl} .

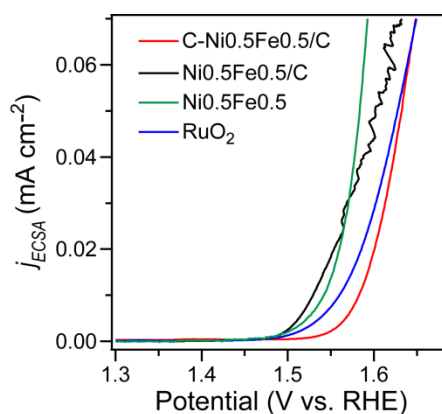


Fig. S17 ECSA normalized activities of Ni_{0.5}Fe_{0.5}/C, Ni_{0.5}Fe_{0.5}, C-Ni_{0.5}Fe_{0.5}/C, and RuO₂. In comparison with Ni_{0.5}Fe_{0.5}, the lower j_{ECSA} of Ni_{0.5}Fe_{0.5}/C at high overpotential arises from the block of active sites by oxygen bubbles, which is reflected by the fluctuation of j_{ECSA} curve. Since the Ni_{0.5}Fe_{0.5}/C has higher intrinsic activity, the oxygen formation speed surpasses the release speed and thus oxygen bubbles can be formed on Ni_{0.5}Fe_{0.5}/C at high overpotential. In contrast, Ni_{0.5}Fe_{0.5} has lower intrinsic activity. The lower oxygen produced speed cannot form oxygen bubbles at active sites.

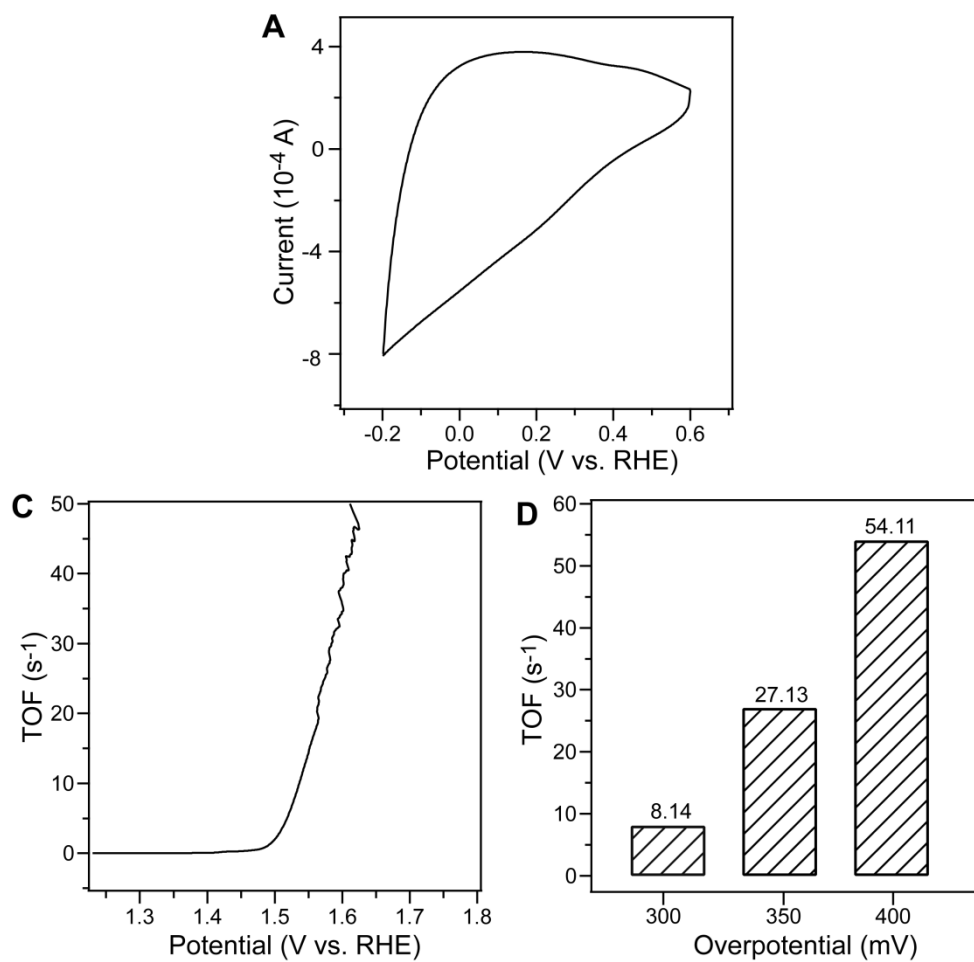


Fig. S18 A) CV curve of Ni_{0.5}Fe_{0.5}/C in 1 M PBS solution. B) TOF of Ni_{0.5}Fe_{0.5}/C with respect to potential. C) Specific TOF at three typical overpotentials.

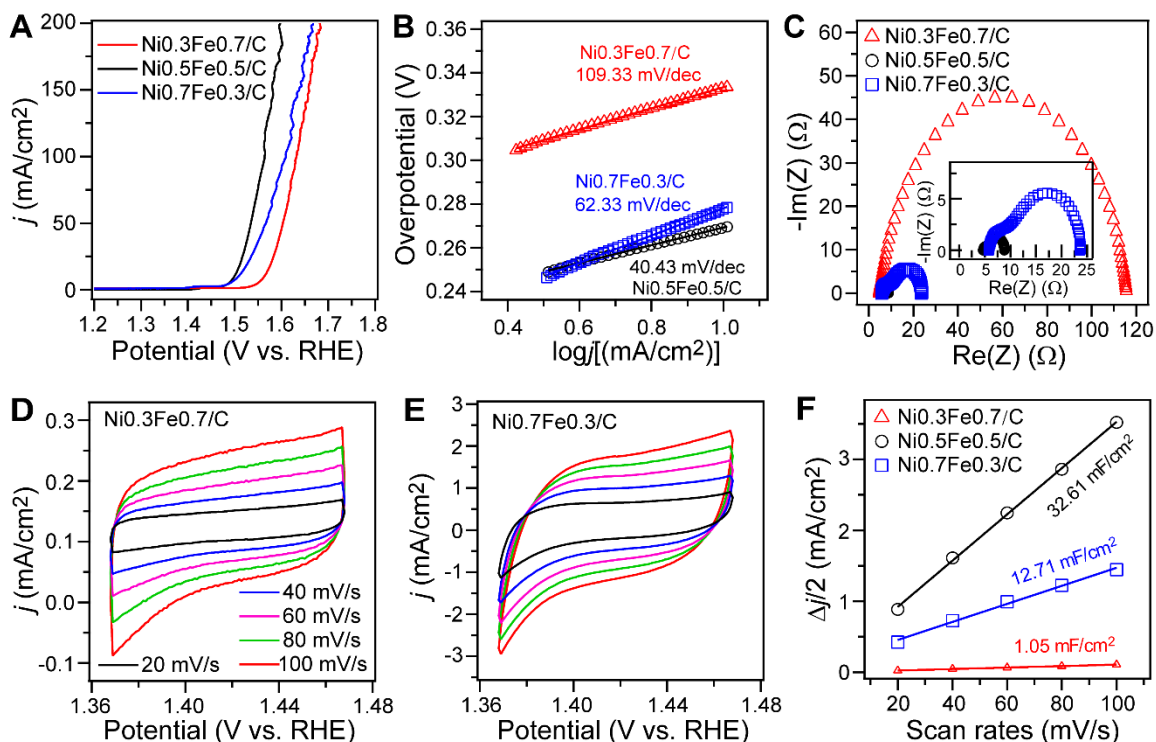


Fig. S19 OER performances of Ni_{0.3}Fe_{0.7}/C, Ni_{0.5}Fe_{0.5}/C, and Ni_{0.7}Fe_{0.3}/C in 1 M KOH electrolyte. A) Polarization curves with scan rate of 5 mV/s. B) Tafel plots. C) Nyquist impedance curves. D, E) CV curves of Ni_{0.3}Fe_{0.7}/C and Ni_{0.7}Fe_{0.3}/C under different scanning speeds, respectively. F) Charging current density differences plotted against scan rates. Charging current density differences are obtained at 1.42 V vs. RHE.

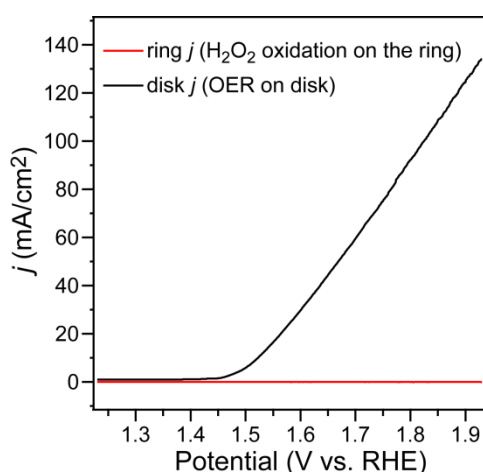


Fig. S20 RRDE LSV curve of Ni_{0.5}Fe_{0.5}/C. The applied potential onto Pt-ring is 1.5 V vs. RHE.

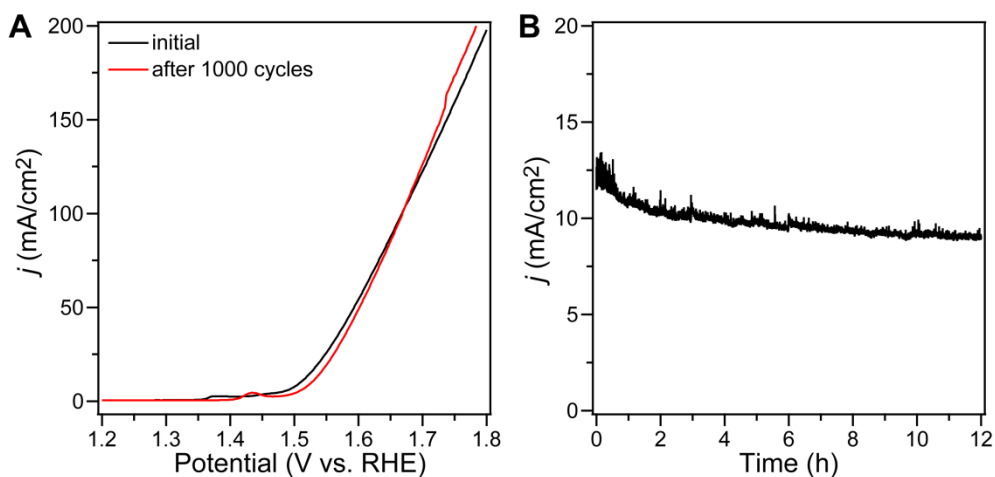


Fig. S21 A) Polarization curves of Ni_{0.5}Fe_{0.5}/C recorded initially and after 1000 CV sweeps between 1.273 and 1.722 V vs. RHE with scan rate of 100 mV/s. B) Chronoamperometric curves of Ni_{0.5}Fe_{0.5}/C at 1.512 V vs. RHE.

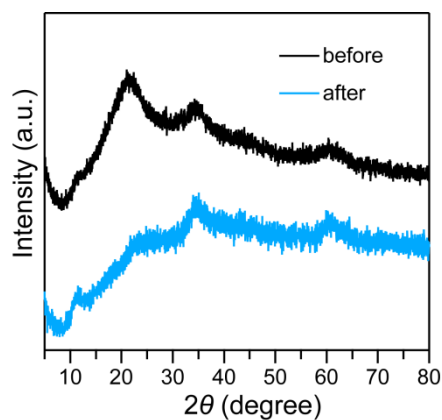


Fig. S22 XRD patterns of Ni_{0.5}Fe_{0.5}/C before and after 10-h stability measurement.

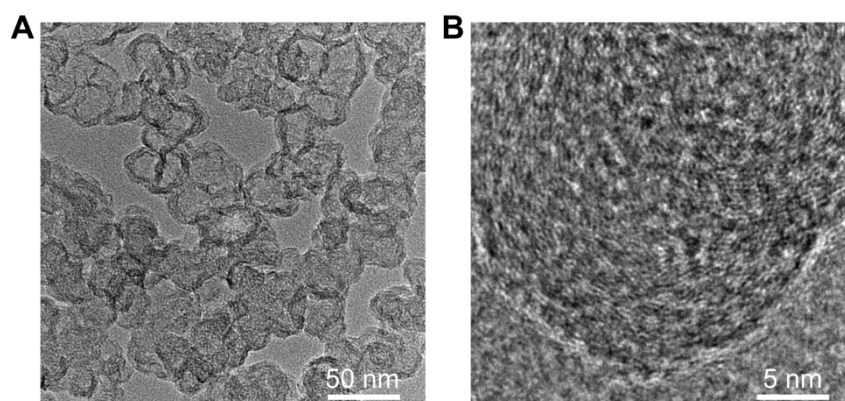


Fig. S23 A) TEM and B) HRTEM images of Ni_{0.5}Fe_{0.5}/C after 10-h stability measurement.

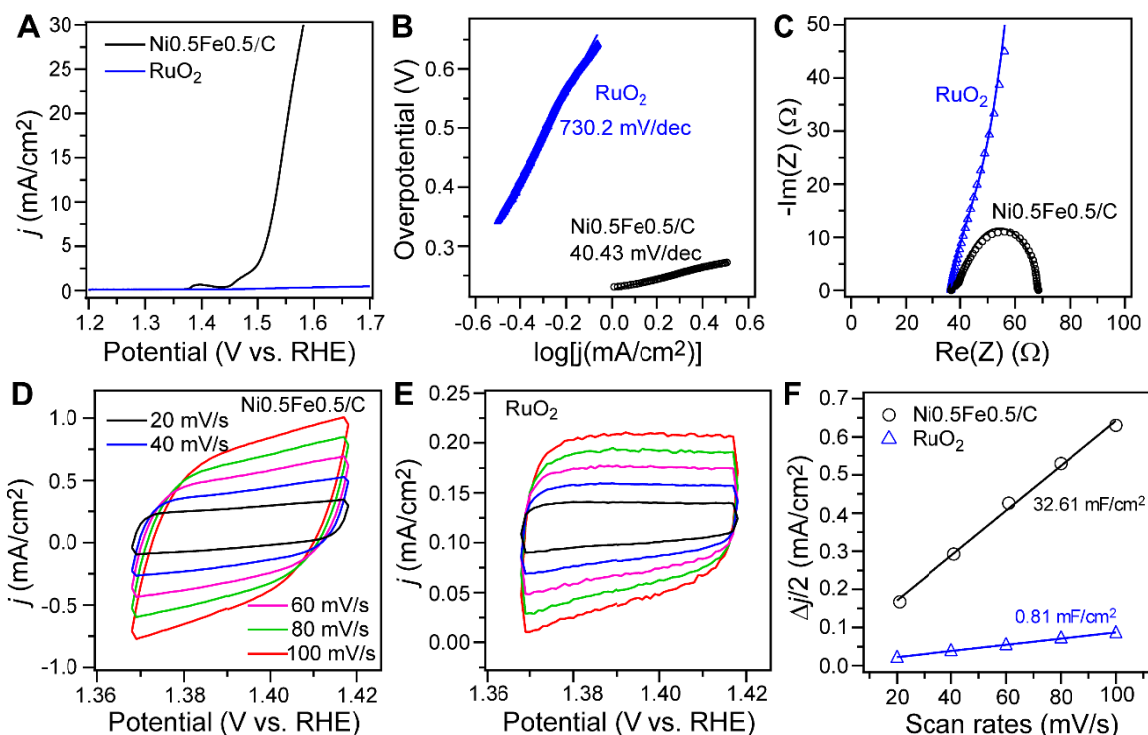


Fig. S24 OER performances of Ni_{0.5}Fe_{0.5}/C and commercial RuO₂ catalyst in 0.1 M KOH electrolyte. A) Polarization curves with scan rate of 5 mV/s. B) Tafel plots. C) Nyquist impedance curves. D, E) CV curves of Ni_{0.5}Fe_{0.5}/C and commercial RuO₂ catalyst under different scanning speeds, respectively. F) Charging current density differences plotted against scan rates. Charging current density differences are obtained at 1.39 V vs. RHE.

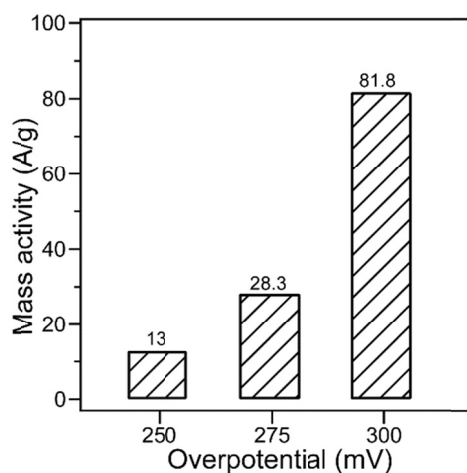


Fig. S25 Mass activity of Ni_{0.5}Fe_{0.5}/C in 0.1 M KOH solution.

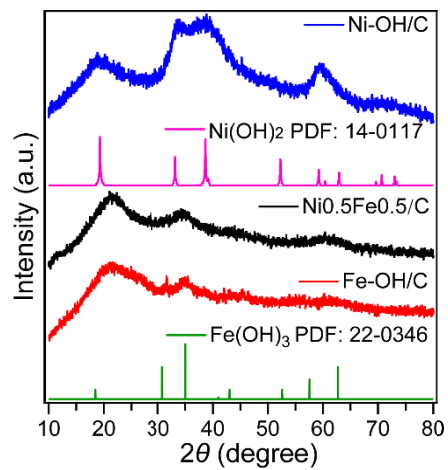


Fig. S26 XRD patterns of Fe-OH/C and Ni-OH/C.

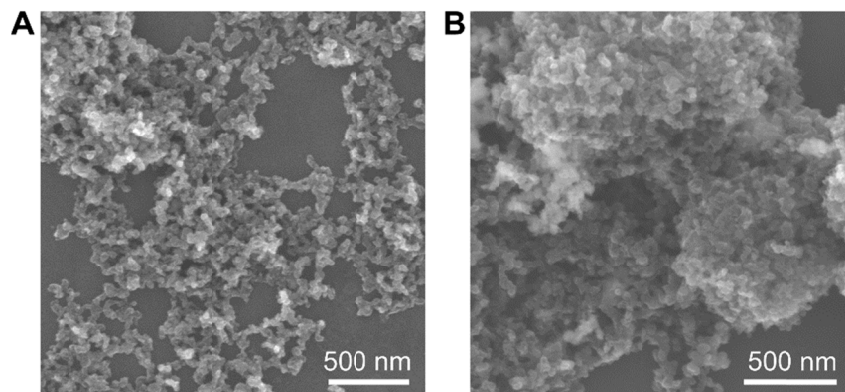


Fig. S27 A,B) SEM images of Fe-OH/C and Ni-OH/C, respectively.

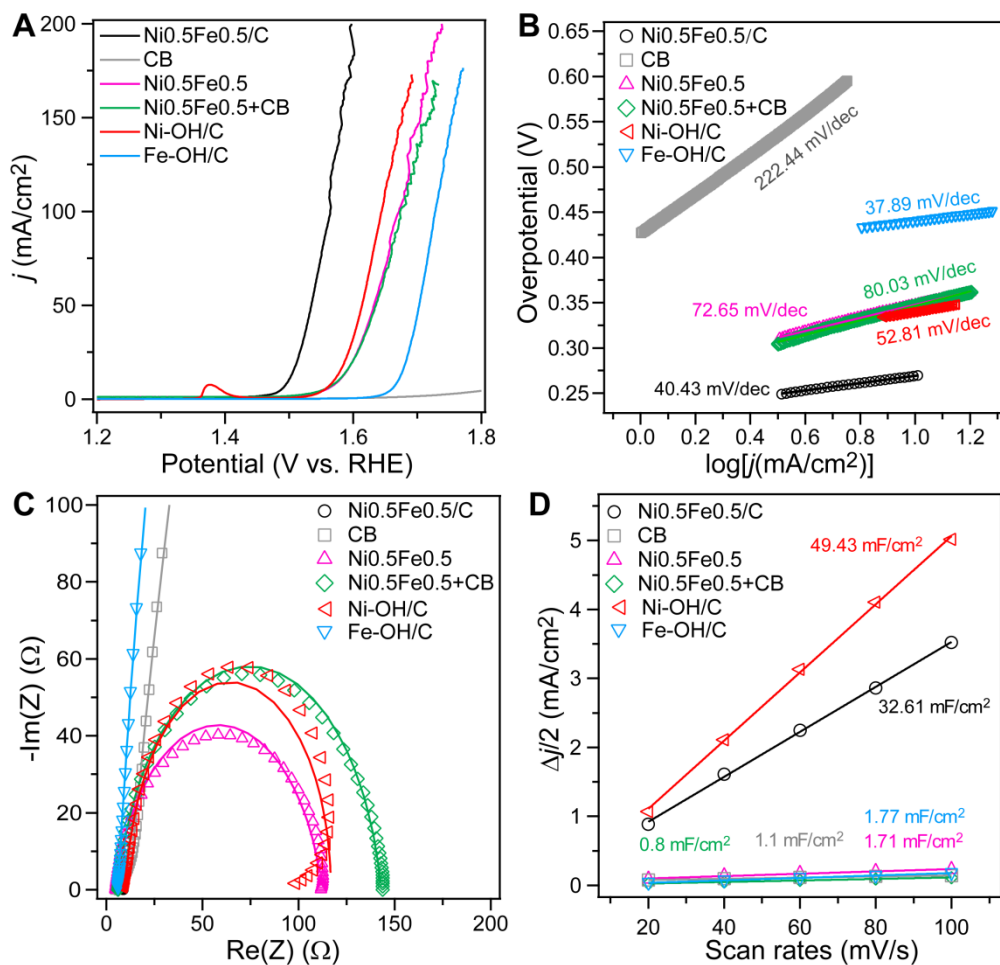


Fig. S28 OER performances of different samples. A) Polarization curves with scan rate of 5 mV/s. B) Tafel plots. C) Nyquist impedance curves. D) Charging current density differences plotted against scan rates. Charging current density differences are obtained at 1.42 V vs. RHE.

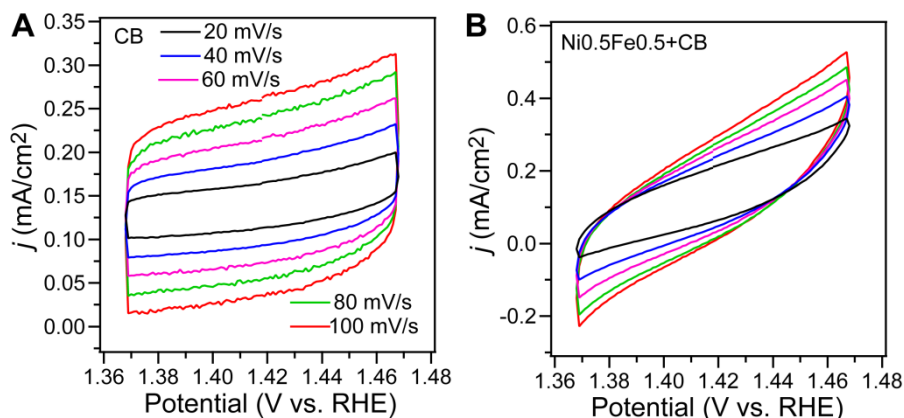


Fig. S29 A-C) CV curves of CB, Ni0.5Fe0.5, and Ni0.5Fe0.5+CB under different scanning speeds, respectively.

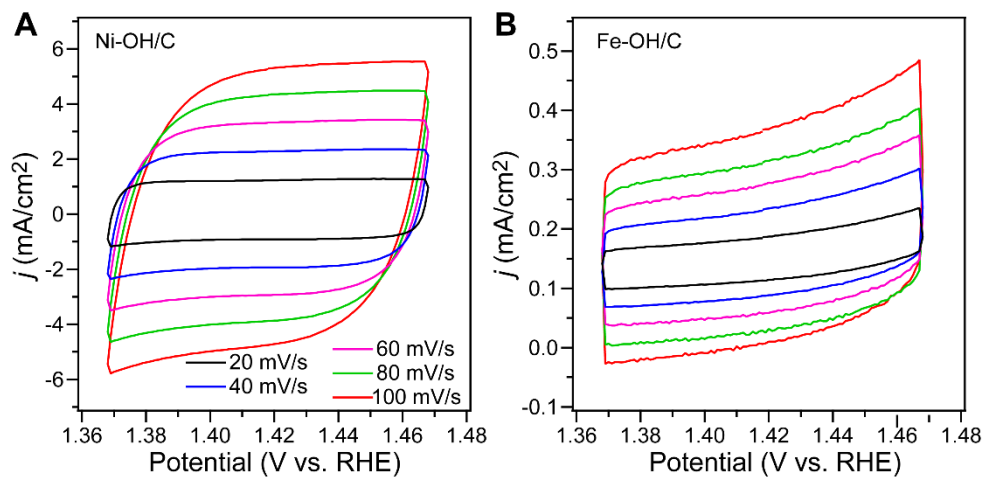


Fig. S30 A,B) CV curves of Ni-OH/C and Fe-OH/C under different scanning speeds, respectively.

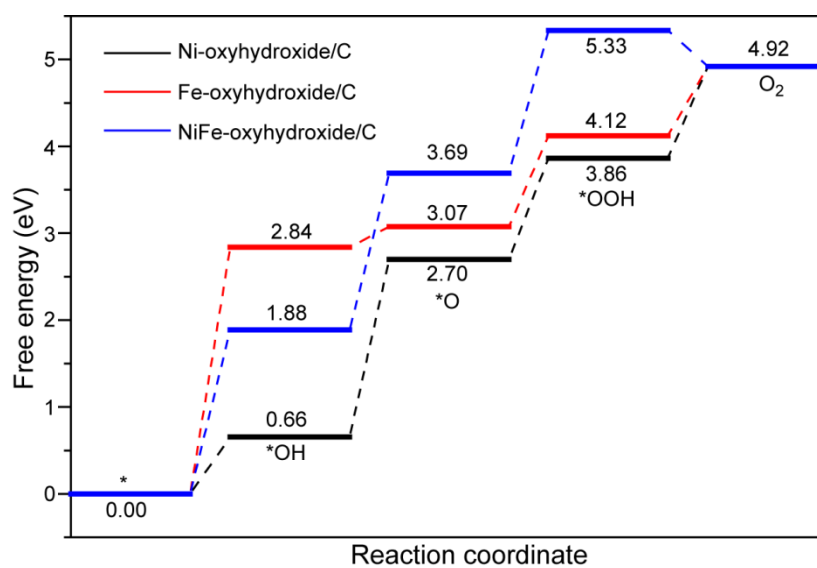


Fig. S31 Free-energy diagram for oxygen evolution reaction on Ni-OH/C, Fe-OH/C, and Ni_{0.5}Fe_{0.5}/C at potential of 0.00 V vs. RHE. The numbers are the free energy of the involved species, with unit of eV.

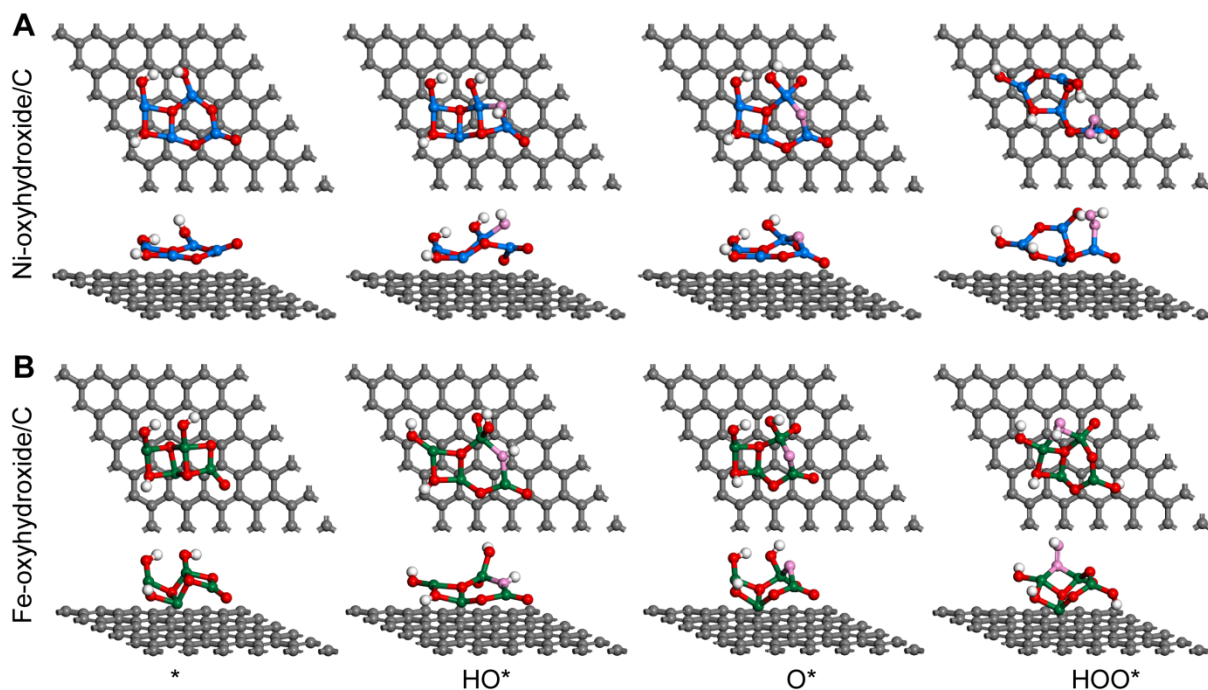


Fig. S32 Top and side views of adsorption configurations of OER intermediates on A) Ni(OH)₂/C and B) Fe(OH)₂/C. The blue, green, grey, and white spheres represent Ni, Fe, C, and H atoms, respectively. The red and pink spheres represent the lattice O of NiFe-oxyhydroxide cluster and the reactive O in ORR process.

Table S1. Comparison of OER performance between Ni_{0.5}Fe_{0.5}/C and other reported transition metal based electrocatalysts in 1-M KOH

samples	mass loading (mg/cm ²)	substrate	η @10 mA/cm ² (mV)	Tafel slope (mV/dec)	Reference
Ni _{0.5} Fe _{0.5} /C	0.128	GC ^b	269.55	40.43	This work
Ni _{0.5} Fe _{0.5} /C ^a	0.128	GC ^b	300.46	92	This work
Co _{0.7} Fe _{0.3} CB	N.A.	GC ^b	295	36.2	<i>Adv. Funct. Mater.</i> 2020 , 1909889.
Fe-Co ₉ S ₈ @SNC	0.51	GC ^b	273	55.8	<i>Nano Res.</i> , 2022 , 15, 872.
Reduced NiCo ₂ O ₄ NPs	2.5	NF ^c	240	50	<i>J. Am. Chem. Soc.</i> 2018 , 140, 13644.
Mn ₃ N ₂	3	NF ^c	270	101	<i>Angew. Chem., Int. Ed.</i> 2018 , 57, 698.
NiCo ₂ O ₄ hollow nanostructure	0.6	CB ^d	340	72	<i>Adv. Energy Mater.</i> 2017 , 7, 1602391.
Ni _x Fe _{1-x} OOH/NiFe/ Ni _x Fe _{1-x} OOH	1	CB ^d	220	57	<i>ACS Appl. Mater. Interfaces</i> 2017 , 9, 34954
NiFe-PBA (V _{CN})	0.255	GC ^b	283	54	<i>Nat. Commun.</i> 2019 , 10, 2799.
a-NiFeMo oxide ^a	0.25	GC ^b	280	49	<i>Angew. Chem. Int. Ed.</i> 2019 , 58, 15772.
CoFe-LDH (V _{Co} , V _{Fe} , V _O)	0.204	GC ^b	290	36	<i>Adv. Mater.</i> 2017 , 29, 1701546.
Ni-Fe LDH hollow nanoprisms	0.16	GC ^b	280	49.4	<i>Angew. Chem. Int. Ed.</i> 2018 , 57, 172.
W ₂ N/WC	N.A.	GC ^b	320	94.5	<i>Adv. Mater.</i> 2020 , 32, 1905679.
Co/N-CNT	0.285	GC ^b	310	66	<i>Small</i> 2020 , 16, 2002427.
Fe ₃ C-Co/NC	0.4	GC ^b	340		<i>Adv. Funct. Mater.</i> 2019 , 29, 1901949.
Ag NW@NiMn-LDH (1:2)	0.070	GC ^b	270	40.2	<i>ACS Nano</i> 2020 , 14, 1770.
NiO/Co ₃ O ₄	1.91	NF ^c	262	58	<i>ACS Catal.</i> 2020 , 10, 12376.
NiFe-LDH	N.A.	NF ^c	240	N.A.	<i>Science</i> 2014 , 345, 1593.
FeCoNi-LDH-2	0.255	GC ^b	269	42.34	<i>Adv. Energy Mater.</i> 2021 , 2102141.

CoOx NPs/BNG ^a	N.A.	GC ^b	295	57	<i>Angew. Chem., Int. Ed.</i> 2017 , <i>56</i> , 7121.
NiFe-VOx-0.5	0.25	GC ^b	267	38	<i>Small</i> 2021 , 2105763.
NiFe _{0.5} Sn-A	0.048	^d CB	260	50	<i>Adv. Sci.</i> 2020 , <i>7</i> , 1903777.
NiCo ₂ S ₄ @NiFe LDH ^a	N.A.	GC ^b	287	86.4	<i>Appl. Catal., B</i> 2021 , <i>286</i> , 119869.
Ni-N ₄ /GHSs/Fe-N ₄ ^a	0.26	GC ^b	390	81	<i>Adv. Mater.</i> 2020 , <i>32</i> , 2003134.

^aThe OER performance was conducted in 0.1 M KOH solution. ^bGC is glassy carbon electrode. ^cNF is Nickel foam. ^dCB is carbon cloth.

References

- [1] L. Zeng, K. Sun, X. Wang, Y. Liu, Y. Pan, Z. Liu, D. Cao, Y. Song, S. Liu, C. Liu, *Nano Energy*, **2018**, *51*, 26.
- [2] I. K. Mishra, H. Zhou, J. Sun, F. Qin, K. Dahal, J. Bao, S. Chen, Z. Ren, *Energy Environ. Sci.* **2018**, *11*, 2246.
- [3] Q. Fu, X. Wang, J. Han, J. Zhong, T. Zhang, T. Yao, C. Xu, T. Gao, S. Xi, C. Liang, L. Xu, P. Xu, B. Song, *Angew. Chem. Int. Ed.* **2021**, *60*, 259.
- [4] J. R. Swierk, S. Klaus, L. Trotochaud, A. T. Bell, T. D. Tilley, *J. Phys. Chem. C* **2015**, *119*, 19022.
- [5] G. Kresse, J. Furthmüller, *Phys. Rev. B* **1996**, *54*, 11169.
- [6] G. Kresse, J. Furthmüller, *Comput. Mater. Sci.* **1996**, *6*, 15.
- [7] J. P. Perdew, K. Burke, M. Ernzerhof, *Phys. Rev. Lett.* **1996**, *77*, 3865.
- [8] P. E. Blöchl, *Phys. Rev. B* **1994**, *50*, 17953.
- [9] G. Kresse, D. Joubert, *Phys. Rev. B* **1999**, *59*, 1758.
- [10] S. Grimme, S. Ehrlich, L. Goerigk, *J. Comput. Chem.* **2011**, *32*, 1456.
- [11] M.-F. Ng, D. J. Blackwood, H. Jin, T. L. Tan, *J. Phys. Chem. C* **2020**, *124*, 13799.
- [12] P. Liao, J. A. Keith, E. A. Carter, *J. Am. Chem. Soc.* **2012**, *134*, 13296.